DRAFT VERSION JANUARY 26, 2022
Typeset using LaTeX **twocolumn** style in AASTeX631

Schwarzschild and Ledoux are equivalent on evolutionary timescales

EVAN H. ANDERS,[1,2] ADAM S. JERMYN,[3,2] DANIEL LECOANET,[1,4,2] ADRIAN E. FRASER,[5,2] IMOGEN G. CRESSWELL,[6,2] AND J. R. FUENTES[7]

[1] *CIERA, Northwestern University, Evanston IL 60201, USA*
[2] *Kavli Institute for Theoretical Physics, University of California, Santa Barbara, CA 93106, USA*
[3] *Center for Computational Astrophysics, Flatiron Institute, New York, NY 10010, USA*
[4] *Department of Engineering Sciences and Applied Mathematics, Northwestern University, Evanston IL 60208, USA*
[5] *University of California, Santa Cruz, Santa Cruz, California 95064, U.S.A*
[6] *Department Astrophysical and Planetary Sciences & LASP, University of Colorado, Boulder, CO 80309, USA*
[7] *Department of Physics and McGill Space Institute, McGill University, 3600 rue University, Montreal, QC H3A 2T8, Canada*

(Received July 28, 2021; Revised October 19, 2021; Accepted; Published)

Submitted to ApJ

ABSTRACT

This will be an abstract.

Keywords: UAT keywords

1. INTRODUCTION

Observations tell us we don't understand the mixing at convective boundaries. For example, models and observations disagree about the sizes of convective cores (Claret & Torres 2018; Viani & Basu 2020; **?**), lithium abundances in solar-type stars (Pinsonneault 1997; Sestito & Randich 2005; Carlos et al. 2019; Dumont et al. 2021), and there is a well-known acoustic glitch in helioseismology at the base of the convection zone (see Basu 2016, Sec. 7.2.1). Improperly calculating the size of a convection zone can have important impacts across astrophysics such as setting the mass of stellar remnants (Farmer et al. 2019; Mehta et al. 2022) and affecting the inferred radii of exoplanets (Basu et al. 2012; Morrell 2020).

While there are many undercertainties in convective boundary mixing (CBM), the most fundamental question is: what sets the nominal boundary of the CZ? One way of answering this question is by evaluating the *Schwarzschild criterion*, which determines where the temperature and pressure stratification within a star are stable or unstable. The other answer is the *Ledoux criterion*, which accounts for stability or instability due to the composition (e.g., the variation of helium abundance with pressure; see Salaris & Cassisi 2017, chapter 3, for a nice review of these criteria). Recent work states that these criteria are logically equivalent at a convective boundary in the mixing length formalism (Gabriel et al. 2014; Paxton et al. 2018, 2019), but they are not always implemented to be that way (as in early versions of the MESA instrument, Paxton et al. 2013).

Modern studies still have not reached a consensus of which criterion to employ (see Kaiser et al. 2020, chapter 2, for a brief discussion). Multi-dimensional simulations have demonstrated that convection zones with Ledoux-stable boundaries expand by entraining compositionally-stable regions (Meakin & Arnett 2007; Woodward et al. 2015; Jones et al. 2017; Cristini et al. 2019; Fuentes & Cumming 2020; Andrassy et al. 2020, 2021). However, it is unclear from past 3D simulations whether that entrainment should stop at a Schwarzschild-stable boundary, leading to uncertainty in how to model entrainment in 1D models (Staritsin 2013; Scott et al. 2021).

In this work, we present a simple 3D hydrodynamical simulation that demonstrates that convection zones with Ledoux-stable but Schwarzschild-unstable boundaries will entrain material over roughly a thermal timescale until both the Ledoux and Schwarzschild criteria are equivalent at the convective boundary. Therefore, in 1D stellar evolution models, when the evolution time

Corresponding author: Evan H. Anders
evan.anders@northwestern.edu

is greater than or roughly equal to the thermal time (such as on the main sequence, see Georgy et al. 2021), these criteria should be implemented so that either one produces the same evolution. We briefly discuss these criteria in Sec. 2, display our simulations in Sec. **??**, and provide a brief discussion in Sec. 4.

2. THEORY & EXPERIMENT

The stability of a convective region can instantaneously be determined using the Schwarzschild criterion,

$$\mathcal{Y}_{\rm S} = \nabla_{\rm rad} - \nabla_{\rm ad}, \tag{1}$$

or the Ledoux criterion,

$$\mathcal{Y}_{\rm L} = \mathcal{Y}_{\rm S} + \frac{\chi_\mu}{\chi_T}\nabla_\mu \tag{2}$$

Here, the temperature gradient $\nabla \equiv d\ln P/d\ln T$ has a value of $\nabla_{\rm ad}$ for an adiabatic stratification and $\nabla_{\rm rad}$ if all flux is carried through radiative conductivity. The composition gradient $\nabla_\mu = d\ln\mu/d\ln P$ is multiplied by the ratio of $\chi_T = (d\ln P/d\ln T)_{\rho,\mu}$ and $\chi_\mu = (d\ln P/d\ln\mu)_{\rho,T}$, where ρ is the density, T is the temperature, P is the pressure, and μ is the mean molecular weight.

In Eqns. 1 and 2, $\mathcal{Y}$ is the discriminant (e.g., Paxton et al. 2018, sec. 2), related to the superadiabaticity. In stellar structure codes, convective boundaries are assumed to coincide with sign changes in the discriminant. The various stability regimes which can occur in stars are well-described in section 3 and figure 3 of Salaris & Cassisi (2017), but we will briefly recap four important regimes:

1. Convection Zones (CZs): If $\mathcal{Y}_{\rm S} > 0$ and $\mathcal{Y}_{\rm L} \geq \mathcal{Y}_{\rm S}$, a region's stratification is convectively unstable.

2. Radiative Zones (RZs): If both $\mathcal{Y}_{\rm S} < 0$ and $\mathcal{Y}_{\rm L} < \mathcal{Y}_{\rm S}$, a region's stratification is stable to convection.

3. "Semiconvection" zone: If $\mathcal{Y}_{\rm S} > 0$ but $\mathcal{Y}_{\rm L} < 0$, a stable composition gradient stabilizes an unstable thermal stratification. These regions can be linearly unstable to overstable doubly diffusive convection (ODDC, see Garaud 2018, chapter 2), or they can be stable RZs.

4. "Thermohaline" zone: If $\mathcal{Y}_{\rm S} < 0$ and $\mathcal{Y}_{\rm L} > \mathcal{Y}_{\rm S}$, a stable thermal stratification stabilizes an unstable composition gradient. These regions can be linearly unstable to thermohaline mixing or fingering convection (see Garaud 2018, chapter 3), or they can be stable RZs.

In this paper, we study 3D simulations of a linearly-stable semiconvection zone (#3) bounded below by a CZ (#1) and above by an RZ (#2). We examine how the boundary of the CZ evolves through entrainment. In particular, we are interested in seeing if $\mathcal{Y}_{\rm S}$ and $\mathcal{Y}_{\rm L}$ evolve towards the same height due to entrainment. Since stellar evolution timesteps generally span many convective overturn times, our 3D simulation should evolve to the proper state, which may be quite different from our initial conditions.

In this work, we utilize a simplified 3D model which employs the Boussinesq approximation, which assumes that the depth of the layer being studied is much smaller than the local scale height. Since we are studying thin regions near convective boundaries, this assumption is OK. The relevant physics for this problem are included ($\nabla_{\rm rad}$ varies with height, buoyancy is determined both by the composition C and the temperature stratification T), so $\mathcal{Y}_{\rm S}$ and $\mathcal{Y}_{\rm L}$ are meaningfuly defined and distinct from one another when composition gradients are present. For details on our model setup and Dedalus simulations, we refer the reader to appendices A and B.

3. RESULTS

Volume visualizations of simulation dynamics are shown near the initial state (left) and evolved state (right) in Fig. 1. Buoyancy perturbations normalized by the vertical profile of buoyancy standard deviations are shown in the top two panels. Vertical velocity is shown in the bottom two panels. In the initial state, convection occurs in the bottom $\sim 1/3$ of the simulation domain; the middle $\sim 1/3$ of the domain is stabilized by a composition gradient, and the top $\sim 1/3$ is stabilized by a thermal gradient. The convection excites gravity waves in the stable layers. The Brunt-Väisälä frequency is higher by a factor of 10 in the thermal layer than in the semiconvection layer, so the vertical velocity signature of motions there is smaller than in the semiconvection layer. Describe overhoot.

The most obvious difference between the panels on the left and the right is that the convection zone has grown in size from $\sim 1/3$ of the simulation domain to $\sim 2/3$ of the simulation domain. Through continuous overshoot, convection entrained stable, low-composition fluid from the upper region into the convection zone. This process eroded the composition gradient until the Schwarzschild and Ledoux boundaries of the convection zone were identical. In other words, the *thermal* stability of the upper zone is sufficient to halt expansion of the convection zone via entrainment, but compositional stability is not. We see negligible convective penetration (mixing of the bouyancy or entropy profile beyond the

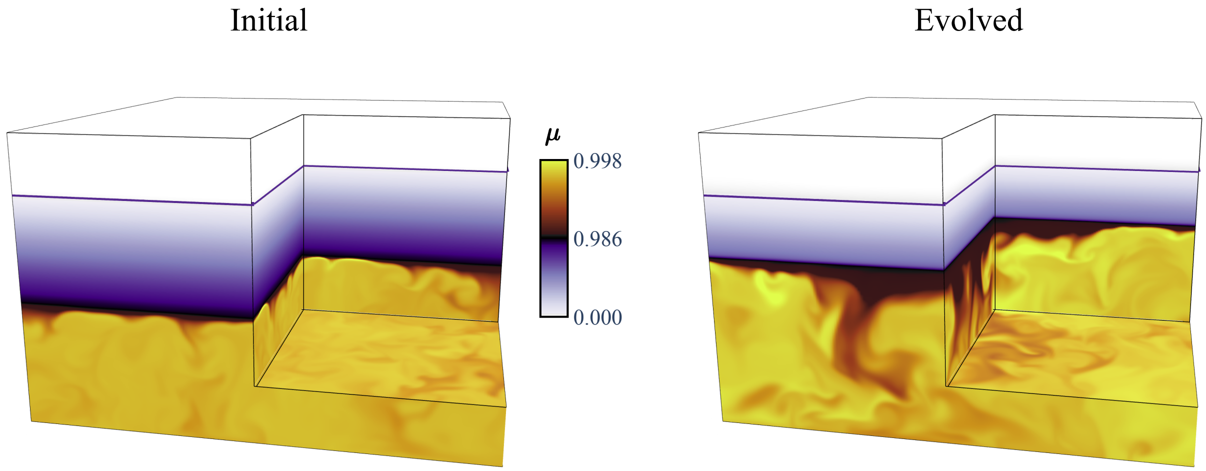

Figure 1.

sign change in $mathcalY$), but this is expected and part of our experimental design (see appendix).

Figure 2 displays vertical profiles that have been averaged horizontally and in time. Profiles on the left show initial conditions, while profiles on the right show the evolved state. We show the composition (top panels), the Schwarzschild and Ledoux discriminants (middle panels), and the square Brunt-Väisälä and convective frequencies.

In the initial state, we see that the composition is uniform in the CZ ($z \leq 1$) and RZ ($z \geq 2$), but varies linearly in $z \in [1, 2]$ and provides stability. We also see that the sign change in $\mathcal{Y}_{\rm L}$ occurs at $z \sim 1$ while that in $\mathcal{Y}_{\rm S}$ occurs at $z \sim 2$. Finally, we see that $f_{\rm conv} = 0$ because we initialize the simulation without any convective velocity. However, the Brunt-Väisälä frequency N^2 is negative in a boundary layer at the base of the CZ which drives the instability, and N^2 is stable above $z = 1$ (and is more stable by a factor of 10 above $z \sim 2$).

The final state (right) is attained after convection entrains and mixes through the initial composition gradient. We see that the composition profile (top) is constant in the convection zone, and approximates a step function above the CZ at the top of the overshoot zone. (TODO: Add overshoot to this figure). In this evolved state, the sign changes in the discriminants $\mathcal{Y}_{\rm L}$ and $\mathcal{Y}_{\rm S}$ coincide (middle panel). In the bottom panel, we see that the convective frequency is roughly constant, and see that $N^2 \lesssim 0$ in the bulk CZ. We can compute the "stiffness" $\mathcal{S} = N^2/f_{\rm conv}^2$ of the radiative-convective boundary by comparing the average CZ value of $f_{\rm conv}^2 \sim 10^{-2}$ to the RZ value of $N^2 \sim 10^2$, so $\mathcal{S} \approx 10^4$. Boundaries with a low stiffness $\mathcal{S} \lesssim 10$ easily deform in the presence of convective flows, but convective boundaries in stars often have $\mathcal{S} \gtrsim 10^6$. The value of $\mathcal{S}$ achieved in these simulations is therefore in the right regime to tell us about stars, but these simulations still exhibit more mechanical overshoot than we would expect stars to.

Finally, In figure 3, we plot a Kippenhahn-like diagram of the simulation. The CZ is shown in orange and is the region below the sign change of both and $\mathcal{S}$. The semiconvection zone is shown in green and is the region below the sign changes of and $\mathcal{S}$. The RZ is shown in purple and is the region above the sign change of both and $\mathcal{S}$. Convection overshoot roughly above the $\mathcal{Y}_{\rm L} = 0$ line up to the black line, denoted by a hashed region. The height of the black line traces out the region where the vertical profile of the convective kinetic energy falls below 10% of its value in the bulk CZ; this line roughly coincides with the extremum of the composition gradient through the simulation evolution. Importantly, while the orange line that traces out $\mathcal{Y}_{\rm L} = 0$ and the green line tracing out $\mathcal{Y}_{\rm S} = 0$ start at different heights, 3D convective motions make these lines converge on long timescales.

4. CONCLUSIONS & DISCUSSION

In this letter, we present 3D simulations of a convection zone and its boundary. The initial boundary is

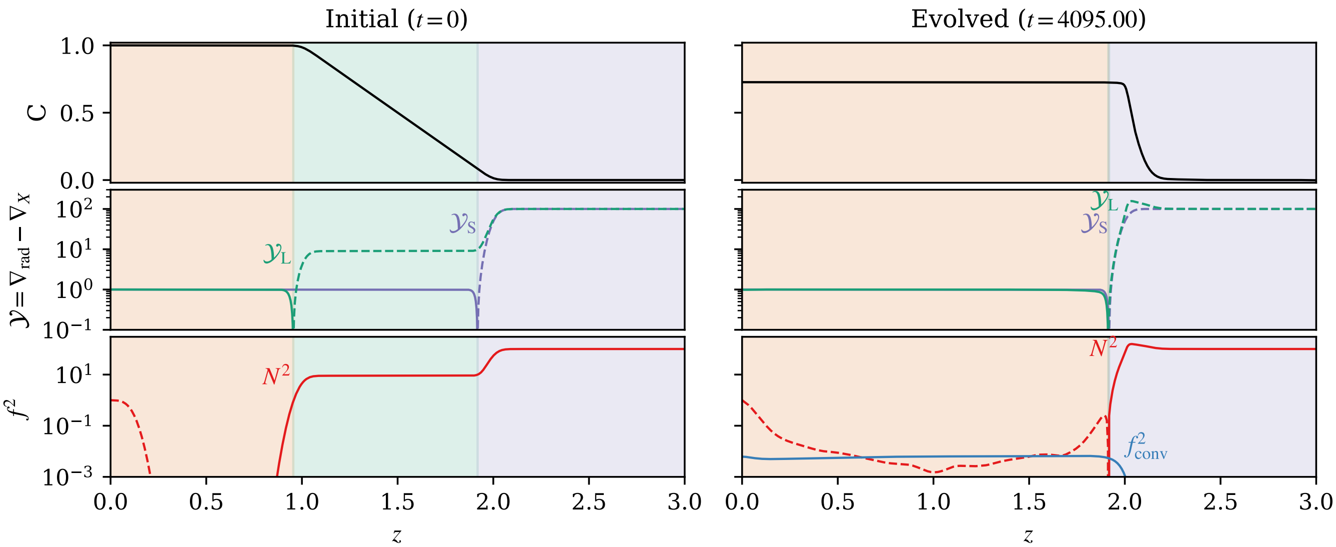

Figure 2.

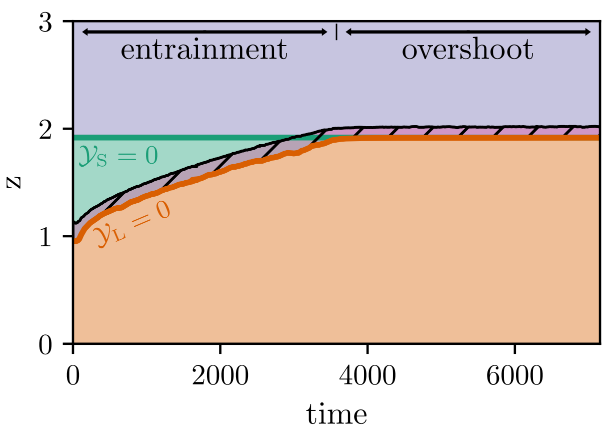

Figure 3.

compositionally stable but weakly thermally unstable (Ledoux stable but Schwarzschild unstable). Entrainment causes the convective boundary to advance until the Ledoux and Schwarzschild criterion agree upon the location of the convective boundary.

These simulations demonstrate that the Ledoux criterion properly defines the *instantaneous* criterion for the boundary of a convection zone. However, when the evolutionary timescale $t_{\rm evolution} \gg t_{\rm conv}$, the convective overturn timescale, the Schwarzschild criterion provides the best description of the steady-state boundary of the convection zone. Our 3D dynamical simulations support the claim that "logically consistent" implementations of mixing length theory (Gabriel et al. 2014; Paxton et al. 2018, 2019) must set the Schwarzschild discriminant $\mathcal{Y}_{\rm S}=0$ at the convective boundary. This suggests that the MESA software instrument's modern "convective pre-mixing" (CPM) algorithm should properly find the boundary of most convection zones. Put differently, our simulations suggest that 1D stellar evolution models should not produce different answers when using the Schwarzschild or Ledoux criterion for convective stability when $t_{\rm evolution} \gg t_{\rm conv}$.

We note briefly that many Ledoux-stable but Schwarzschild-unstable regions in stars are unstable to overstable doubly-diffusive convection (ODDC). ODDC generally mixes more quickly than the entrainment studied here, and has been studied extensively in local simulations (Mirouh et al. 2012; Wood et al. 2013; Xie et al. 2017); see Garaud (2018) for a nice review. ODDC has been applied in 1D stellar evolution models to the regions near main sequence stellar convective cores in Moore & Garaud (2016). They find rapid mixing of ledoux-stable but schwarzschild-unstable regions, and ODDC formulations should should be widely included in stellar models.

For stages in stellar evolution where $t_{\rm conv} \sim t_{\rm evolution}$, implementations of time-dependent convection (TDC, CITE) should be employed to properly capture convective dynamics and the advancement of convective boundaries. The advancement of convective boundaries in TDC implementations should be informed by time-dependent theories and simulations of the motion of convective boundaries (e.g., Turner 1968; Fuentes & Cumming 2020).

The purpose of this study was to understand how the root of the discriminant $\mathcal{Y}_{\rm L}$ evolves over time, and whether it coincides with the root of $\mathcal{Y}_{\rm S}$ at late times. While there is interesting behavior near the boundary beyond that point (e.g., mechanical convective overshoot), a detailed analysis of that phenomenon is beyond the scope of this work. We furthermore constructed the simulations in this work to have a small penetration parameter $\mathcal{P}$ (**?**) and we see negliglble convective penetration in our simulations. Finally, in our simulations, the radiative conductivity is independent of the magnitude of the composition μ, but this is not the case in stars. Since the radiative conductivity sets the location of the Schwarzschild boundary, including these effects would change the exact location of our final convective boundary, but would not change the fundamental takeaways of this work.

In summary, we find that the Schwarzschild criterion provides the location of the convective boundary in a statistically stationary state; in this final state, the Ledoux and Schwarzschild criteria are degenerate.

We thank Meridith Joyce, Anne Thoul, Dominic Bowman, Jared Goldberg, Tim Cunningham, Falk Herwig, Kyle Augustson, (OTHERS?) for useful discussions which helped improve our understanding. EHA is funded as a CIERA Postdoctoral fellow and would like to thank CIERA and Northwestern University. This research was supported in part by the National Science Foundation under Grant No. PHY-1748958, and we acknowledge the hospitality of KITP during the Probes of Transport in Stars Program. Computations were conducted with support from the NASA High End Computing (HEC) Program through the NASA Advanced Supercomputing (NAS) Division at Ames Research Center on Pleiades with allocation GID s2276. The Flatiron Institute is supported by the Simons Foundation.

APPENDIX

A. MODEL & INITIAL CONDITIONS

In this work we study the simplest possible system: incompressible, Boussinesq convection with a composition field and a height-varying background radiative conductivity, similar to that used in Fuentes & Cumming (2020); Anders et al. (2021). These equations are

$$\boldsymbol{\nabla}\cdot\boldsymbol{u} = 0, \tag{A1}$$

$$\partial_t\boldsymbol{u}\cdot\boldsymbol{\nabla}\boldsymbol{u} = -\frac{1}{\rho_0}\boldsymbol{\nabla}p + \frac{\rho_1}{\rho_0}\boldsymbol{g} + \nu\boldsymbol{\nabla}^2\boldsymbol{u}, \tag{A2}$$

$$\partial_t T + \boldsymbol{u}\cdot\boldsymbol{\nabla}T + w\nabla_{\mathrm{ad}} + \boldsymbol{\nabla}\cdot[-\kappa_{T,0}\boldsymbol{\nabla}\overline{T}] = \kappa_T\boldsymbol{\nabla}^2 T', \tag{A3}$$

$$\partial_t C + \boldsymbol{u}\cdot\boldsymbol{\nabla}C = \kappa_{C,0}\boldsymbol{\nabla}^2\overline{C} + \kappa_C\boldsymbol{\nabla}^2 C', \tag{A4}$$

$$\frac{\rho_1}{\rho_0} = -|\alpha|T + |\beta|C. \tag{A5}$$

Here, $\boldsymbol{u}$ is the vector velocity, T is the temperature, C is the composition, ρ_0 is the constant background density, p is the kinematic pressure which enforces Eqn. A1, ρ_1 are density fluctuations which act only on the buoyant term, and α and β are the thermal and compositional expansion coefficients, and ∇_{ad} is the adiabatic gradient. Diffusive terms are controlled by the kinematic viscosity ν, as well as the thermal diffusivity κ_T and compositional diffusivity κ_C. On the horizontally-invariant ($n_x = 0$ and $n_y = 0$) mode, we use a height-depended thermal diffusion coefficient $\kappa_{T,0}$ (which allows $\nabla_{\rm rad}$ to vary with height) and a lower compositional diffusivity $\kappa_{C,0} < \kappa_C$ to ensure that the evolution of the mean composition profile is due to advection rather than diffusion.

We nondimensionalize Eqns. A1-A5 according to

$$\begin{aligned} &T^* = (\Delta T)T, \qquad C^* = (\Delta C)C, \qquad \partial_{t^*} = \tau_{\rm ff}^{-1}\partial_t, \qquad \boldsymbol{\nabla}^* = L_s^{-1}\boldsymbol{\nabla}, \qquad p^* = \rho_0 u_{\rm ff}^2 \varpi, \\ &\boldsymbol{u}^* = u_{\rm ff}\boldsymbol{u} = \frac{L_s}{\tau_{\rm ff}}\boldsymbol{u}, \qquad \tau_{\rm ff} = \left(\frac{L_s}{|\alpha| g \Delta T}\right)^{1/2}, \qquad \kappa_{T,0}^* = (L_s^2 \tau_{\rm ff}^{-1})\kappa_{T,0}. \end{aligned} \tag{A6}$$

For convenience, here we define quantities with $*$ (e.g., T^*) as being the "dimensionful" quantities of Eqns. A1-A5. Henceforth, quantities without $*$ (e.g., T) are dimensionless. Here, L_s is the length scale of the initial Schwarzschild-unstable convection zone and $\tau_f f$ is the buoyant freefall timescale. The temperature and composition are set by the destabilizing radiative temperature gradient $\Delta T = L_s(\partial_z T + \boldsymbol{\nabla}_{\rm ad})$ and the stabilizing composition gradient ($\Delta C = L_s \partial_z C$). Within this nondimensionalization, the dynamical control parameters are

$$\mathcal{P} = \frac{u_{\rm ff} L_s}{\kappa_T}, \qquad \mathrm{R}_0 = \frac{|\alpha|\Delta T}{|\beta|\Delta C}, \qquad \mathrm{Pr} = \frac{\nu}{\kappa_T}, \qquad \tau = \frac{\kappa_C}{\kappa_T}, \qquad \tau_0 = \frac{\kappa_{C,0}}{\kappa_T} \tag{A7}$$

The dimensionless equations of motion are

$$\boldsymbol{\nabla}\cdot\boldsymbol{u} = 0 \tag{A8}$$

$$\partial_t \boldsymbol{u} + \boldsymbol{u}\cdot\boldsymbol{\nabla}\boldsymbol{u} = -\boldsymbol{\nabla}\varpi + (T - \mathrm{R}_0^{-1}C)\hat{z} + \frac{\mathrm{Pr}}{\mathcal{P}}\boldsymbol{\nabla}^2\boldsymbol{u} \tag{A9}$$

$$\partial_t T + \boldsymbol{u}\cdot\boldsymbol{\nabla}T + w\boldsymbol{\nabla}_{\rm ad} + \boldsymbol{\nabla}\cdot[-\kappa_{T,0}\boldsymbol{\nabla}\overline{T}] = \frac{1}{\mathcal{P}}\boldsymbol{\nabla}^2 T'., \tag{A10}$$

$$\partial_t C + \boldsymbol{u}\cdot\boldsymbol{\nabla}C = -\frac{\tau_0}{\mathcal{P}}\boldsymbol{\nabla}^2\overline{C} + \frac{\tau}{\mathcal{P}}\boldsymbol{\nabla}^2 C'. \tag{A11}$$

We define the thermal and compositional gradients

$$\nabla_{\rm T} \equiv -\frac{\partial T}{\partial z}, \qquad \nabla_{\rm C} \equiv -\mathrm{R}_0^{-1}\frac{\partial C}{\partial z}, \tag{A12}$$

and stability is determined by the sign of the Brunt-Väisälä frequency,

$$N^2 = N^2_{\rm structure} + N^2_{\rm composition}, \text{ with } N^2_{\rm structure} = -(\nabla_{\rm T} - \nabla_{\rm ad}),\ N^2_{\rm composition} = \nabla_{\rm C}, \tag{A13}$$

where $N^2 > 0$ is buoyantly stable, so the stability criterion is $\nabla_{\rm C} - (\nabla_{\rm T} - \nabla_{\rm ad}) > 0$, as in stellar models (Salaris & Cassisi 2017).

In this work, we study a three-layer model in $z = [0, 3]$. We want to construct a simulation with

$$N^2 = \begin{cases} -1 & z \leq 1 \\ R_0^{-1} - 1 & 1 < z \leq 2 \\ R_0^{-1} & 2 < z \end{cases}, \qquad N^2_{\rm composition} = \begin{cases} 0 & z \leq 1 \\ R_0^{-1} & 1 < z \leq 2 \\ 0 & 2 < z \end{cases}, \qquad N^2_{\rm structure} = \begin{cases} -1 & z \leq 1 \\ -1 & 1 < z \leq 2 \\ R_0^{-1} & 2 < z \end{cases} \tag{A14}$$

To achieve this, we set $\partial_z C = -\mathrm{R}_0 N^2_{\rm composition}$ and $\partial_z T = N^2_{\rm structure} - \nabla_{\rm ad}$, where we set $\nabla_{\rm ad} = 5[\mathrm{R}_0^{-1} - 2]$ as a constant so that $\nabla_{\rm ad} > 0$ for all values of R_0 studied. We furthermore enforce that $\nabla_{\rm T} = \nabla_{\rm rad}$ in the initial state, where

$$\nabla_{\rm rad} = -\frac{F_{\rm tot}}{\kappa_{T,0}}, \tag{A15}$$

is the radiative gradient and $F_{\rm tot}$ is the total vertical energy flux through the system. We set the total flux $F_{\rm tot} = -(1 + \nabla_{\rm ad})/\mathcal{P}$ and the convective flux $F_{\rm conv} = 1/\mathcal{P}$, so $\kappa_{T,0}(z) = -((1 + \nabla_{\rm ad})/\partial_z T)\mathcal{P}^{-1}$.

B. SIMULATION DETAILS & DATA AVAILABILITY

We time-evolve equations ?? using the Dedalus pseudospectral solver (Burns et al. 2020) using timestepper SBDF2 (Wang & Ruuth 2008) and safety factor 0.3. All fields are represented as spectral expansions of n_z Chebyshev coefficients in the vertical (z) direction and as (n_x, n_y) Fourier coefficients in the horizontal (x, y) directions; our domain is therefore horizontally periodic. We use a domain with an aspect ratio of two so that $x \in [0, L_x]$, $y \in [0, L_y]$, and $z \in [0, L_z]$ with $L_x = L_y = 2L_z$. The initial convection zone spans initially spans 1/3 of the domain depth and in the evolved state spans 2/3 of the domain depth, so it has an initial aspect ratio of 6 and a final aspect ratio of 3. To avoid aliasing errors, we use the 3/2-dealiasing rule in all directions. To start our simulations, we add random noise temperature perturbations with a magnitude of 10^{-6} to the initial temperature profile (discussed in ??).

Spectral methods with finite coefficient expansions cannot capture true discontinuities. In order to approximate discontinuous functions such as Eqns. A14, we must use smooth transitions. We therefore define a smooth Heaviside step function,

$$H(z; z_0, d_w) = \frac{1}{2}\left(1 + \text{erf}\left[\frac{z - z_0}{d_w}\right]\right). \tag{B16}$$

where erf is the error function. In the limit that $d_w \to 0$, this function behaves identically to the classical Heaviside function centered at z_0. Throughout this work, we set $d_w = 0.05$.

A table describing all of the simulations presented in this work can be found in Appendix C. We produce figures ?? and ?? using matplotlib (Hunter 2007; Caswell et al. 2021). We produce figure ?? using TODO. All of the Python scripts used to run the simulations in this paper and to create the figures in this paper are publicly available in a git repository[1], and in a Zenodo repository (**?**).

C. TABLE OF SIMULATION PARAMETERS

Input parameters and summary statistics of the simulations presented in this work are shown in Table **??**.

REFERENCES

Anders, E. H., Jermyn, A. S., Lecoanet, D., & Brown, B. P. 2021, arXiv e-prints, arXiv:2110.11356. https://arxiv.org/abs/2110.11356

Andrassy, R., Herwig, F., Woodward, P., & Ritter, C. 2020, MNRAS, 491, 972, doi: 10.1093/mnras/stz2952

Andrassy, R., Higl, J., Mao, H., et al. 2021, arXiv e-prints, arXiv:2111.01165. https://arxiv.org/abs/2111.01165

Basu, S. 2016, Living Reviews in Solar Physics, 13, 2, doi: 10.1007/s41116-016-0003-4

Basu, S., Verner, G. A., Chaplin, W. J., & Elsworth, Y. 2012, ApJ, 746, 76, doi: 10.1088/0004-637X/746/1/76

Burns, K. J., Vasil, G. M., Oishi, J. S., Lecoanet, D., & Brown, B. P. 2020, Physical Review Research, 2, 023068, doi: 10.1103/PhysRevResearch.2.023068

Carlos, M., Meléndez, J., Spina, L., et al. 2019, MNRAS, 485, 4052, doi: 10.1093/mnras/stz681

Caswell, T. A., Droettboom, M., Lee, A., et al. 2021, matplotlib/matplotlib: REL: v3.3.4, v3.3.4, Zenodo, doi: 10.5281/zenodo.4475376

Claret, A., & Torres, G. 2018, ApJ, 859, 100, doi: 10.3847/1538-4357/aabd35

[1] https://github.com/evanhanders/convective_penetration_paper

Cristini, A., Hirschi, R., Meakin, C., et al. 2019, MNRAS, 484, 4645, doi: 10.1093/mnras/stz312

Dumont, T., Palacios, A., Charbonnel, C., et al. 2021, A&A, 646, A48, doi: 10.1051/0004-6361/202039515

Farmer, R., Renzo, M., de Mink, S. E., Marchant, P., & Justham, S. 2019, ApJ, 887, 53, doi: 10.3847/1538-4357/ab518b

Fuentes, J. R., & Cumming, A. 2020, Physical Review Fluids, 5, 124501, doi: 10.1103/PhysRevFluids.5.124501

Gabriel, M., Noels, A., Montalbán, J., & Miglio, A. 2014, A&A, 569, A63, doi: 10.1051/0004-6361/201423442

Garaud, P. 2018, Annual Review of Fluid Mechanics, 50, 275, doi: 10.1146/annurev-fluid-122316-045234

Georgy, C., Saio, H., & Meynet, G. 2021, A&A, 650, A128, doi: 10.1051/0004-6361/202040105

Hunter, J. D. 2007, Computing in Science and Engineering, 9, 90, doi: 10.1109/MCSE.2007.55

Jones, S., Andrassy, R., Sandalski, S., et al. 2017, MNRAS, 465, 2991, doi: 10.1093/mnras/stw2783

Kaiser, E. A., Hirschi, R., Arnett, W. D., et al. 2020, MNRAS, 496, 1967, doi: 10.1093/mnras/staa1595

Meakin, C. A., & Arnett, D. 2007, ApJ, 667, 448, doi: 10.1086/520318

Mehta, A. K., Buonanno, A., Gair, J., et al. 2022, ApJ, 924, 39, doi: 10.3847/1538-4357/ac3130

Mirouh, G. M., Garaud, P., Stellmach, S., Traxler, A. L., & Wood, T. S. 2012, ApJ, 750, 61, doi: 10.1088/0004-637X/750/1/61

Moore, K., & Garaud, P. 2016, ApJ, 817, 54, doi: 10.3847/0004-637X/817/1/54

Morrell, S. A. F. 2020, PhD thesis, University of Exeter

Paxton, B., Cantiello, M., Arras, P., et al. 2013, ApJS, 208, 4, doi: 10.1088/0067-0049/208/1/4

Paxton, B., Schwab, J., Bauer, E. B., et al. 2018, ApJS, 234, 34, doi: 10.3847/1538-4365/aaa5a8

Paxton, B., Smolec, R., Schwab, J., et al. 2019, ApJS, 243, 10, doi: 10.3847/1538-4365/ab2241

Pinsonneault, M. 1997, ARA&A, 35, 557, doi: 10.1146/annurev.astro.35.1.557

Salaris, M., & Cassisi, S. 2017, Royal Society Open Science, 4, 170192, doi: 10.1098/rsos.170192

Scott, L. J. A., Hirschi, R., Georgy, C., et al. 2021, MNRAS, 503, 4208, doi: 10.1093/mnras/stab752

Sestito, P., & Randich, S. 2005, A&A, 442, 615, doi: 10.1051/0004-6361:20053482

Staritsin, E. I. 2013, Astronomy Reports, 57, 380, doi: 10.1134/S1063772913050089

Turner, J. S. 1968, Journal of Fluid Mechanics, 33, 183, doi: 10.1017/S0022112068002442

Viani, L. S., & Basu, S. 2020, ApJ, 904, 22, doi: 10.3847/1538-4357/abba17

Wang, D., & Ruuth, S. J. 2008, Journal of Computational Mathematics, 26, 838. http://www.jstor.org/stable/43693484

Wood, T. S., Garaud, P., & Stellmach, S. 2013, ApJ, 768, 157, doi: 10.1088/0004-637X/768/2/157

Woodward, P. R., Herwig, F., & Lin, P.-H. 2015, ApJ, 798, 49, doi: 10.1088/0004-637X/798/1/49

Xie, J.-H., Miquel, B., Julien, K., & Knobloch, E. 2017, Fluids, 2, doi: 10.3390/fluids2010006